76th International Astronautical Congress (IAC), Sydney, Australia, 29 Sep-3 Oct 2025.

IAC–25–C1,4,7,x99550

Relative reachable domain for spacecraft under uncertainty of time-varying atmospheric density

Nayu Nonomiya[a*], Yasuhiro Yoshimura[b], Toshiya Hanada[c]

[a]*Kyushu University, 744 Motooka, Nishi-ku, Fukuoka, 819-0395, Japan*, nonomiya.nayu.184@s.kyushu-u.ac.jp
[b]*Kyushu University, 744 Motooka, Nishi-ku, Fukuoka, 819-0395, Japan*,
[c]*Kyushu University, 744 Motooka, Nishi-ku, Fukuoka, 819-0395, Japan*,
*Corresponding Author

Abstract

The growing congestion in low Earth orbit (LEO) demands robust frameworks to evaluate satellite relative motion under uncertainty. The relative reachable domain (RRD) provides a powerful tool to characterize the set of possible relative trajectories; however, conventional formulations neglect atmospheric drag, limiting their applicability in LEO. This study extends the RRD framework by explicitly incorporating atmospheric density uncertainty and the nonlinear effect of differential drag. A quasi-numerical approach is developed that combines nonlinear propagation with envelope extraction, which enables a continuous and interpretable description of the RRD boundary. The proposed method bridges the gap between linearized analytical models and full-scale simulations, enhancing the ability to visualize and quantify uncertainty in relative motion. The resulting framework contributes to more realistic collision risk assessment and supports safer orbit design in the increasingly crowded LEO environment.

Keywords: Relative Reachable Domain, Differential Drag, Atmospheric Density Uncertainty, Collision Risk Assessment,

1. Introduction

The number of space objects in near-Earth orbit has increased rapidly due to advances in space development, leading to growing concerns regarding orbital safety, collision avoidance, and long-term sustainability. In this context, space situational awareness (SSA) has become increasingly important [1, 2]. Scenarios involving proximity operations or cluster flights with a large number of satellites require advanced monitoring and control to accurately determine their positions and to prevent collisions [3–8]. However, such operations are inevitably subject to measurement and operational errors, which are difficult to completely eliminate. These errors, especially in the context of satellite relative motion, can cause deviations from the nominal orbit and increase the risk of collision. Addressing these issues requires precise prediction of satellite positions and relative behaviors, which remains a key challenge in SSA [9].

One promising framework to address these challenges is the relative reachable domain (RRD) [10–13], which characterizes the set of possible relative positions achievable under uncertain dynamics. RRD analysis provides valuable insights for collision risk assessment, formation maintenance, and debris avoidance strategies. In low Earth orbit (LEO), atmospheric drag plays a dominant role in predicting satellite trajectories [3–5]. Since drag strongly depends on satellite geometry and attitude, differential drag significantly affects relative motion and has even been exploited as a control mechanism in distributed satellite systems. However, conventional RRD studies focus on initial state uncertainties and neglect drag effects [10], limiting their applicability to relative motion in LEO [5].

This study extends the RRD framework by explicitly incorporating differential drag and its uncertainty. Based on a transition-matrix formulation, the proposed method integrates nonlinear propagation and boundary extraction through numerical optimization. This enables a continuous and interpretable description of RRD boundaries that more accurately reflects relative motion under atmospheric drag.

2. Preliminaries

2.1 Relative Reachable Domain

The concept of the reachable set (RS) originates from control theory and provides a fundamental tool for analyzing spacecraft dynamics under uncertainty [12, 13]. The RS is defined as the set of all states that a spacecraft can attain within a specified time interval from a given initial condition. In the context of relative motion, RS analysis is particularly important for two reasons: 1) to evaluate the operational capability of the spacecraft and plan missions accordingly, and 2) to predict the operational boundaries of neighboring spacecraft from which collision probabilities can be effectively monitored to improve the level of situational awareness.

The reachable domain (RD) generalizes this concept by considering the union of all reachable sets over arbitrary time. In other words, while the RS characterizes the states reachable at a particular time horizon, the RD represents the overall maneuverability of a spacecraft wiihtout time

horizon limitation. Extending this concept to satellite relative motion leads to the definition of the relative reachable domain (RRD). The RRD geometrically represents the set of possible relative positions that arise due to uncertainties in the initial state and environmental conditions, such as measurement errors or atmospheric drag variations. Thus, the RD describes the maneuverability of a single spacecraft in an absolute sense, whereas the RRD describes the uncertainty-driven dispersion of relative trajectories. The relationship between the RS and the RD is illustrated schematically in Fig. 1. The ellipses denote RSs at different time intervals, while the shaded region corresponds to the RD. Essentially, the RD can be interpreted as the envelope of RSs evolving over time, providing a continuous and comprehensive representation of uncertainty in relative motion.

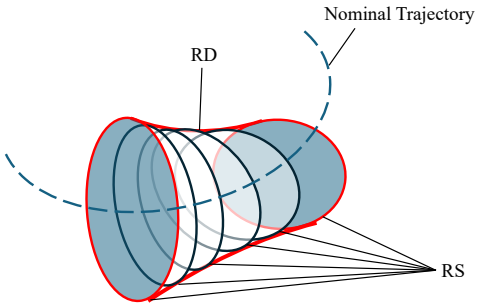

Fig. 1: Relation between the RD and the RS.

2.2 Relative Motion Dynamics

For a deputy satellite with respect to a chief in a circular reference orbit of radius R, the relative dynamics in the Hill frame can be expressed by the Clohessy–Wiltshire (CW) equations as follows:

$$\ddot{x} - 2n\dot{y} - 3n^2 x = u_x \tag{1}$$

$$\ddot{y} + 2n\dot{x} = u_y \tag{2}$$

$$\ddot{z} + n^2 z = u_z \tag{3}$$

where $\boldsymbol{r} = [x, y, z]^T$ and $\boldsymbol{v} = [x, y, z]^T$ are the relative position and velocity, n is the mean motion of chief satellite, and $\boldsymbol{u} = [u_x, u_y, u_z]^T$ represents perturbation accelerations. The general solution can be written using the state transition matrix (STM) $\Phi(t)$ and the convolution kernel $\Psi(t)$ as [8]

$$\begin{bmatrix} \boldsymbol{r}(t) \\ \boldsymbol{v}(t) \end{bmatrix} = \Phi(t) \begin{bmatrix} \boldsymbol{r}(0) \\ \boldsymbol{v}(0) \end{bmatrix} + \Psi(t)\boldsymbol{u}. \tag{4}$$

The drag acceleration on a satellite is given by

$$\boldsymbol{F}_{\text{drag}} = -\frac{1}{2}\frac{C_D A}{m}\rho \, \|\boldsymbol{v}_{\text{rel}}\|\boldsymbol{v}_{\text{rel}} \tag{5}$$

where C_D is the drag coefficient, A the cross-sectional area, m the mass, and $\boldsymbol{v}_{\text{rel}}$ the velocity relative to the atmosphere. The difference in drag accelerations between the chief and deputy yields the differential drag as [2]

$$\begin{aligned} \Delta\boldsymbol{F}_{\text{drag}} = &\frac{1}{2}\frac{C_{D,d}A_d}{M_d}\rho_d\|\boldsymbol{v}_{\text{rel},d}\|\boldsymbol{v}_{\text{rel},d} \\ &-\frac{1}{2}\frac{C_{D,c}A_c}{M_c}\rho_c\|\boldsymbol{v}_{\text{rel},c}\|\boldsymbol{v}_{\text{rel},c} \end{aligned} \tag{6}$$

where the subscript d and c denote the deputy and chief satellite, respectively. The differential drag serves as the primary perturbation driving the evolution of the RRD in LEO [4, 5, 14, 15].

2.3 Problem Setup and Assumptions

Let the nominal relative position and velocity of deputy with respect to chief in the reference LVLH frame be $\boldsymbol{r}_n(t)$ and $\boldsymbol{v}_n(t)$, with initial states $\boldsymbol{r}_{n0}$ and $\boldsymbol{v}_{n0}$. In practice, initial state uncertainties $\delta\boldsymbol{r}_0$ and $\delta\boldsymbol{v}_0$ arise due to measurement and control errors. In the two-dimensional coplanar motion, the RRD appears as an area surrounding the nominal trajectory. Let $\mathcal{S}$ denote the envelope (boundary) of the RRD in the LVLH frame. Once $\mathcal{S}$ is obtained, the RRD corresponds to the region enclosed by $\mathcal{S}$, as illustrated in Fig. 2. The envelope depends on the bounds assigned to the initial uncertainties.

The following assumptions are considered in this study:

1. The nominal relative trajectory lies in a plane that is coplanar with the reference orbital plane (2-D coplanar case).
2. Initial state uncertainties are confined to this plane.
3. Initial position and velocity uncertainties are modeled as zero-mean, uncorrelated, and isotropic in the plane. Practically, deterministic bounds based on 3-σ radii are adopted, so that the position and velocity error boundaries form circles in the orbital plane.
4. The time span considered is limited to a few orbital periods, so that deviations remain small relative to the nominal motion.
5. Perturbations: only differential atmospheric drag is modeled; other perturbations (e.g., J_2, solar radiation pressure, and third-body effects) are neglected.

3. Methods

3.1 Initial conditions

To obtain the envelope of the RRD, the initial state and atmospheric density with the largest uncertainty are assumed, i.e., the upper bound of the initial state and atmospheric density uncertainty. The boundary of the 3-σ

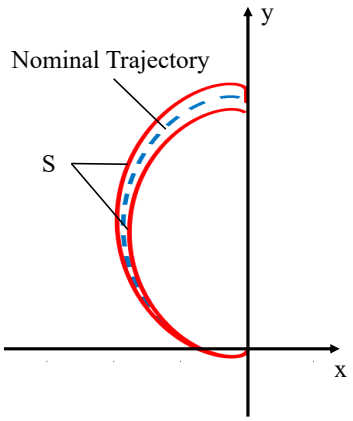

Fig. 2: Geometry of the RRD, envelope of the RRD, and the nominal trajectory.

error is a circle on the orbital plane with radii $\delta \boldsymbol{r}_0$ and $\delta \boldsymbol{v}_0$. As a result, the initial position error and initial velocity error on the boundary circle can be written as

$$\delta \boldsymbol{r}_0(\alpha) = \delta r_0 \begin{bmatrix} \cos\alpha \\ \sin\alpha \end{bmatrix} \tag{7}$$

$$\delta \boldsymbol{v}_0(\beta) = \delta v_0 \begin{bmatrix} \cos\beta \\ \sin\beta \end{bmatrix} \tag{8}$$

where α and β are two angles characterizing the directions of the initial error vectors on the boundary circles.

Atmospheric density is modeled as a nominal value plus an uncertain perturbation as

$$\rho = \rho_0 + \delta\rho(\lambda) \tag{9}$$

where

$$\delta\rho(\lambda) = \delta\rho_0 \tanh(\lambda) \tag{10}$$

The uncertain perturbation is given by $\delta\rho(\lambda)$ and $\delta\rho_0$ denotes the maximum deviation. The parameter λ controls the variation of the uncertain perturbation.

In this manner, the error boundary defined in Eq. (7) and (8) is a rectangle determined by $\delta \boldsymbol{r}_0$ and $\delta \boldsymbol{v}_0$ in Fig. 2. Another commonly used way is to describe the error boundary in the full state space, so that the error boundary is an ellipse in Fig. 3, with semiprincipal axes in the position and velocity subspaces of length $\delta \boldsymbol{r}_0$ and $\delta \boldsymbol{v}_0$, respectively. Obviously, the area of the ellipse is enclosed by the rectangle. Compared to the ellipsoidal error boundary, the rectangular error boundary reduces the number of parameters from three to two, simplifying subsequent RRD calculations.

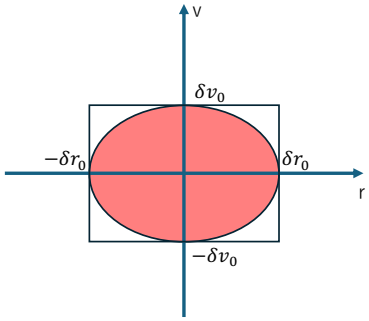

Fig. 3: Two different definitions of the error boundary.

The initial state of the actual motion is written as follows.

$$\boldsymbol{r}_0(\alpha) = \boldsymbol{r}_{n0} + \delta \boldsymbol{r}_0(\alpha) \tag{11}$$

$$\boldsymbol{v}_0(\beta) = \boldsymbol{v}_{n0} + \delta \boldsymbol{v}_0(\beta) \tag{12}$$

Propagated from $\boldsymbol{r}_0(\alpha)$ and $\boldsymbol{v}_0(\beta)$, the actual motion is described by $\boldsymbol{r}(t, \alpha, \beta)$ and $\boldsymbol{v}(t, \alpha, \beta)$. The deviations of the actual motion with respect to the nominal one $\delta \boldsymbol{r}(t, \alpha, \beta)$ and $\delta \boldsymbol{v}(t, \alpha, \beta)$ are expressed as

$$\delta \boldsymbol{r}(t, \alpha, \beta, \lambda) = \boldsymbol{r}(t, \alpha, \beta, \lambda) - \boldsymbol{r}_n(t) \tag{13}$$

$$\delta \boldsymbol{v}(t, \alpha, \beta, \lambda) = \boldsymbol{v}(t, \alpha, \beta, \lambda) + \boldsymbol{v}_n(t) \tag{14}$$

3.2 Nominal Trajectory Propagation

In this study, the nominal relative trajectory is propagated using the full nonlinear equations of motion, including the two-body gravitational dynamics and the atmospheric drag force. While nonlinear propagation has also been employed in previous RRD studies, atmospheric drag effects have not been considered, limiting their applicability in LEO. The differential drag between the chief and deputy, which arises from differences in their area-to-mass ratios, is explicitly incorporated. The equations of motion are given by

$$\ddot{x} - 2\dot{f}\dot{y} - \ddot{f}y - \dot{f}^2 x = -\frac{\mu(R+x)}{[(R+x)^2 + y^2]^{3/2}} + \frac{\mu}{R^2} + \boldsymbol{u}(x) \tag{15}$$

$$\ddot{y} - 2\dot{f}\dot{x} - \ddot{f}x - \dot{f}^2 y = -\frac{\mu y}{[(R+x)^2 + y^2]^{3/2}} + \boldsymbol{u}(y) \tag{16}$$

where μ is the Earth's gravitational parameter, f is the true anomaly, and $\boldsymbol{u}$ is the transformation of $\Delta \boldsymbol{F}_{drag}$ in Eq. (6) from the ECI frame to the LVLH frame. The nominal trajectories of the chief and deputy are propagated numerically using MATLAB `ode45` solver. This nonlinear nominal trajectory serves as the baseline for constructing the RRD.

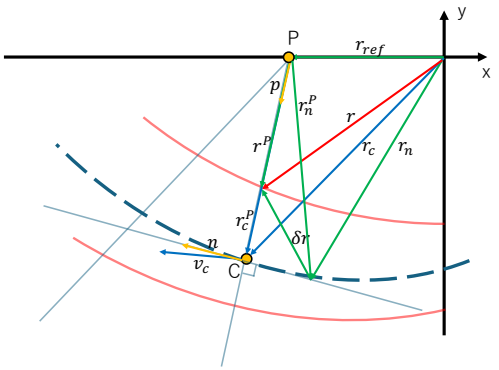

Fig. 4: Geometric definitions for finding the envelope of the RRD.

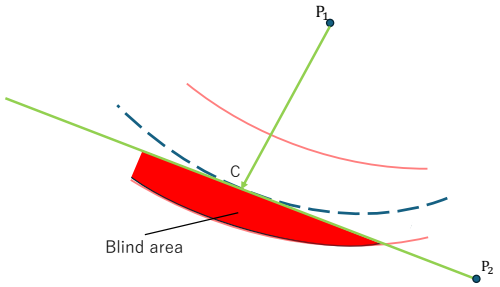

Fig. 5: Blind area.

3.3 RRD Envelope Calculation

The following notations and vectors are defined to find $\mathcal{S}$ (see Fig. 4). Let O be the origin of the reference LVLH coordinate system, C denote a point chosen on the nominal trajectory, t_s be the time in which the nominal trajectory passes through C.The relative position and velocity vectors of the nominal trajectory at point C are $\boldsymbol{r}_c = \boldsymbol{r}_n(t_s)$ and $\boldsymbol{v}_c = \boldsymbol{v}_n(t_s)$, respectively. A given point P is chosen as a reference point to solve the RRD and $\boldsymbol{r}_{\text{ref}}$ is the position vector of P in the reference system. The vector $\boldsymbol{r}_c^p = \boldsymbol{r}_c - \boldsymbol{r}_{\text{ref}}$ denotes the position vector of C relative to P, $\boldsymbol{p}$ is the unit vector of $\boldsymbol{r}_c^p$, expressed as $\boldsymbol{p} = \boldsymbol{r}_c^p / \|\boldsymbol{r}_c^p\|$, and $\boldsymbol{n}$ is a unit vector perpendicular to $\boldsymbol{p}$.

If the reachable boundaries are determined in a given direction $\boldsymbol{p}$, which is specified by the chosen point C and the reference point P, the entire envelope of the RRD is specified by varying the location of C on the nominal trajectory (by varying t_s) and tracing all the boundaries. This is the basic method for finding the envelope of the RRD.

This paper describes the positive vector $\boldsymbol{r}(t,\alpha,\beta,\lambda)$, which can be written as

$$\begin{aligned}\boldsymbol{r}(t,\alpha,\beta,\lambda) &= \boldsymbol{r}_{\text{ref}} + \boldsymbol{r}^p = \boldsymbol{r}_{\text{ref}} + r^p\,\boldsymbol{p} \\ &= \boldsymbol{r}_n(t) + \delta\boldsymbol{r}(t,\alpha,\beta,\lambda)\end{aligned} \tag{17}$$

The construction of the RRD requires specifying reference points along the nominal trajectory. However, if reference points are fixed or placed sparsely, certain regions of the reachable domain may remain uncharacterized, which is referred to as the blind area illustrated in Fig. 5. The presence of blind areas leads to an incomplete representation of the RRD and may underestimate collision risks. Thus, careful selection of reference points is essential to ensure full coverage of the relative reachable set [10].

Note that Eq. (17) imposes a constraint on the time t and the initial uncertainties to ensure that r^p and p are in the same direction. This constraint can be expressed as

$$\begin{aligned}g(t,\alpha,\beta,\lambda) &= \boldsymbol{n}^T\boldsymbol{r}^p \\ &= \boldsymbol{n}^T[\boldsymbol{r}_n(t) - \boldsymbol{r}_{\text{ref}} + \delta\boldsymbol{r}(t,\alpha,\beta,\lambda)] = 0\end{aligned} \tag{18}$$

This shows that the four variables t,α,β,λ are not independent. Actually, only three variables among them are free parameters. If the free parameters are chosen as t, α, and λ, then β is a function of the others, i.e., expressed as $\beta(t,\alpha,\lambda)$. Taking the variation of the constraint function yields

$$\begin{aligned}\delta g &= \delta\{\boldsymbol{n}^T[\boldsymbol{r}_n(t) - \boldsymbol{r}_{\text{ref}} + \delta\boldsymbol{r}(t,\alpha,\beta,\lambda)]\} \\ &= \boldsymbol{n}^T\left[\frac{d\boldsymbol{r}_n(t)}{dt}\delta t + \frac{\partial[\delta\boldsymbol{r}(t,\alpha,\beta,\lambda)]}{\partial t}\delta t\right] + \boldsymbol{n}^T\frac{\partial[\delta\boldsymbol{r}(t,\alpha,\beta,\lambda)]}{\partial\alpha}\delta\alpha\end{aligned} \tag{19}$$

$$+\boldsymbol{n}^T\frac{\partial[\delta\boldsymbol{r}(t,\alpha,\beta,\lambda)]}{\partial\beta}\delta\beta + \boldsymbol{n}^T\frac{\partial[\delta\boldsymbol{r}(t,\alpha,\beta,\lambda)]}{\partial\lambda}\delta\lambda = 0 \tag{20}$$

Thus, the partial derivatives of each variable are given by

$$\frac{\partial\beta(t,\alpha,\lambda)}{\partial\alpha} = -\left[\boldsymbol{n}^T\frac{\partial[\delta\boldsymbol{r}(t,\alpha,\beta,\lambda)]}{\partial\beta}\right]^{-1}\boldsymbol{n}^T\frac{\partial[\delta\boldsymbol{r}(t,\alpha,\beta,\lambda)]}{\partial\alpha} \tag{21}$$

$$\begin{aligned}\frac{\partial\beta(t,\alpha,\lambda)}{\partial t} = &-\left[\boldsymbol{n}^T\frac{\partial[\delta\boldsymbol{r}(t,\alpha,\beta,\lambda)]}{\partial\beta}\right]^{-1} \\ &\cdot\boldsymbol{n}^T\left[\frac{d\boldsymbol{r}_n(t)}{dt}\delta t + \frac{\partial[\delta\boldsymbol{r}(t,\alpha,\beta,\lambda)]}{\partial t}\right]\end{aligned} \tag{22}$$

$$\frac{\partial\beta(t,\alpha,\lambda)}{\partial\lambda} = -\left[\boldsymbol{n}^T\frac{\partial[\delta\boldsymbol{r}(t,\alpha,\beta,\lambda)]}{\partial\beta}\right]^{-1}\boldsymbol{n}^T\frac{\partial[\delta\boldsymbol{r}(t,\alpha,\beta,\lambda)]}{\partial\lambda} \tag{23}$$

Figure 4 indicates that the inner and outer boundaries of the RRD in the direction of $\boldsymbol{p}$ correspond to the minimum

and maximum value of r^p. Thus, if the extrema of the function r^p are specified, then the boundaries are solved. From Eq. (17),

$$\boldsymbol{r}^p = r^p \boldsymbol{p} = \boldsymbol{r}_n(t) + \delta\boldsymbol{r}(t,\alpha,\beta,\lambda) - \boldsymbol{r}_{\text{ref}} \tag{24}$$

Taking the partial derivative yields the following equations

$$\frac{\partial r^p}{\partial t} = \frac{(\boldsymbol{r}^p)^T}{r^p}\frac{\partial \boldsymbol{r}^p}{\partial t} = \boldsymbol{p}^T\frac{\partial \boldsymbol{r}^p}{\partial t} \tag{25}$$

$$\frac{\partial r^p}{\partial \alpha} = \frac{(\boldsymbol{r}^p)^T}{r^p}\frac{\partial \boldsymbol{r}^p}{\partial \alpha} = \boldsymbol{p}^T\frac{\partial \boldsymbol{r}^p}{\partial \alpha} \tag{26}$$

$$\frac{\partial r^p}{\partial \lambda} = \frac{(\boldsymbol{r}^p)^T}{r^p}\frac{\partial \boldsymbol{r}^p}{\partial \lambda} = \boldsymbol{p}^T\frac{\partial \boldsymbol{r}^p}{\partial \lambda} \tag{27}$$

Substituting $\boldsymbol{r}^p$ into Eq.(27) yields

$$\begin{aligned}\frac{\partial r^p}{\partial t} &= \boldsymbol{p}^T\frac{\partial \boldsymbol{r}^p}{\partial t}\\ &= \boldsymbol{p}^T\boldsymbol{V}_r\\ &- \boldsymbol{p}^T\frac{\partial \delta\boldsymbol{r}(t,\alpha,\beta,\lambda)}{\partial\beta}\left[\boldsymbol{n}^T\frac{\partial[\delta\boldsymbol{r}(t,\alpha,\beta,\lambda)]}{\partial\beta}\right]^{-1}\boldsymbol{n}^T\boldsymbol{V}_r\end{aligned} \tag{28}$$

$$\begin{aligned}\frac{\partial r^p}{\partial \alpha} &= \boldsymbol{p}^T\frac{\partial \boldsymbol{r}^p}{\partial \alpha}\\ &= \boldsymbol{p}^T\frac{\partial \delta\boldsymbol{r}(t,\alpha,\beta,\lambda)}{\partial\alpha} - \boldsymbol{p}^T\frac{\partial \delta\boldsymbol{r}(t,\alpha,\beta,\lambda)}{\partial\beta}\\ &\cdot\left[\boldsymbol{n}^T\frac{\partial[\delta\boldsymbol{r}(t,\alpha,\beta,\lambda)]}{\partial\beta}\right]^{-1}\boldsymbol{n}^T\frac{\partial[\delta\boldsymbol{r}(t,\alpha,\beta,\lambda)]}{\partial\alpha}\end{aligned} \tag{29}$$

$$\begin{aligned}\frac{\partial r^p}{\partial \lambda} &= \boldsymbol{p}^T\frac{\partial \boldsymbol{r}^p}{\partial \lambda}\\ &= \boldsymbol{p}^T\frac{\partial \delta\boldsymbol{r}(t,\alpha,\beta,\lambda)}{\partial\lambda} - \boldsymbol{p}^T\frac{\partial \delta\boldsymbol{r}(t,\alpha,\beta,\lambda)}{\partial\beta}\\ &\times\left[\boldsymbol{n}^T\frac{\partial[\delta\boldsymbol{r}(t,\alpha,\beta,\lambda)]}{\partial\beta}\right]^{-1}\boldsymbol{n}^T\frac{\partial[\delta\boldsymbol{r}(t,\alpha,\beta,\lambda)]}{\partial\lambda}\end{aligned} \tag{30}$$

where

$$\boldsymbol{V}_r = \frac{d\boldsymbol{r}_n(t)}{dt}\delta t + \frac{\partial[\delta\boldsymbol{r}(t,\alpha,\beta,\lambda)]}{\partial t} \tag{31}$$

The boundary points can be obtained by finding the critical values of the function r^p. The critical points of the function r^p can be found at the place where the gradient equals zero, that is,

$$\frac{\partial r^p}{\partial t} = 0, \qquad \frac{\partial r^p}{\partial \alpha} = 0, \qquad \frac{\partial r^p}{\partial \lambda} = 0 \tag{32}$$

Define a parameter vector as $\boldsymbol{X} = [t,\alpha,\beta,\lambda]^T$. With the combination of the constraint in Eq. (18) and the zero gradient condition in Eq. (32), the following equation is obtained:

$$\boldsymbol{H}(\boldsymbol{X}) = \begin{bmatrix} g(\boldsymbol{X}) & \frac{\partial r^p}{\partial t} & \frac{\partial r^p}{\partial \alpha} & \frac{\partial r^p}{\partial \lambda}\end{bmatrix}^T = 0 \tag{33}$$

3.4 RRD for Circular Reference Orbits

For circular reference orbits, the state transition matrix for the linearized motion is expressed as

$$\Phi(t) = \begin{bmatrix}\Phi_{11} & \Phi_{12}\\ \Phi_{21} & \Phi_{22}\end{bmatrix} \tag{34}$$

$$\Psi(t) = \begin{bmatrix}\Psi_1\\ \Psi_2\end{bmatrix} \tag{35}$$

where

$$\begin{aligned}\Phi_{11} &= \begin{bmatrix} 4-3\cos nt & 0\\ -6(nt-\sin nt) & 1\end{bmatrix},\\ \Phi_{12} &= \frac{1}{n}\begin{bmatrix}\sin nt & 2(1-\cos nt)\\ 2(\cos nt-1) & 4\sin nt-3nt\end{bmatrix}\\ \Phi_{21} &= \begin{bmatrix} 3n\sin nt & 0\\ -6n(1-\cos nt) & 0\end{bmatrix}\\ \Phi_{22} &= \begin{bmatrix}\cos nt & 2\sin nt\\ -2\sin nt & 4\cos nt-3\end{bmatrix}\end{aligned} \tag{36}$$

$$\begin{aligned}\Psi_1 &= \frac{1}{n^2}\begin{bmatrix} 2\sin^2\frac{nt}{2} & -2\sin nt+2nt\\ 2\sin nt-2nt & 8\sin^2\frac{nt}{2}-\frac{3}{2}n^2t^2\end{bmatrix}\\ \Psi_2 &= \frac{1}{n}\begin{bmatrix}\sin nt & 4\sin^2\frac{nt}{2}\\ -4\sin^2\frac{nt}{2} & -3nt+4\sin nt\end{bmatrix}\end{aligned} \tag{37}$$

The deviation $\delta\boldsymbol{r}$ and $\delta\boldsymbol{v}$ can be modeled by the linearized equations,

$$\delta\boldsymbol{r}(t,\alpha,\beta,\lambda) = \boldsymbol{\Phi}_{11}(t)\delta\boldsymbol{r}_0(\alpha) + \boldsymbol{\Phi}_{12}(t)\delta\boldsymbol{v}_0(\beta) + \boldsymbol{\Psi}_1(t)\delta\boldsymbol{u}(\lambda) \tag{38}$$

$$\delta\boldsymbol{v}(t,\alpha,\beta,\lambda) = \boldsymbol{\Phi}_{21}(t)\delta\boldsymbol{r}_0(\alpha) + \boldsymbol{\Phi}_{22}(t)\delta\boldsymbol{v}_0(\beta) + \boldsymbol{\Psi}_2(t)\delta\boldsymbol{u}(\lambda) \tag{39}$$

where the initial state uncertainties are given by Eq. (12).

The nominal motion at the neighborhood of $\boldsymbol{r_c}$ is approximated as

$$\begin{cases}\boldsymbol{r}_n(t) = \boldsymbol{\Phi}_{11}(t-t_s)\boldsymbol{r}_c + \boldsymbol{\Phi}_{12}(t-t_s)\boldsymbol{v}_c + \boldsymbol{\Psi}_1(t-t_s)\boldsymbol{u}(\lambda)\\ \boldsymbol{v}_n(t) = \boldsymbol{\Phi}_{21}(t-t_s)\boldsymbol{r}_c + \boldsymbol{\Phi}_{22}(t-t_s)\boldsymbol{v}_c + \boldsymbol{\Psi}_2(t-t_s)\boldsymbol{u}(\lambda)\end{cases} \tag{40}$$

where $\boldsymbol{r}_c$ and $\boldsymbol{v}_c$ are solved by propagating the nominal relative motion from $\boldsymbol{r}_{n0}$ and $\boldsymbol{v}_{n0}$ to time t_s using the nonlinear dynamic model in Eq. (16).

The direction vector $\boldsymbol{p}$ is obtained from both $\boldsymbol{r}_c$ and the given $\boldsymbol{r}_{\text{ref}}$ as

$$\boldsymbol{p} = \frac{\boldsymbol{r}_c - \boldsymbol{r}_{\text{ref}}}{\|\boldsymbol{r}_c - \boldsymbol{r}_{\text{ref}}\|} \tag{41}$$

Projecting the unit vectors onto the LVLH frame yields the following equations

$$\boldsymbol{p} = \begin{bmatrix} \cos\nu \\ \sin\nu \end{bmatrix} \tag{42}$$

$$\boldsymbol{n} = \begin{bmatrix} -\sin\nu \\ \cos\nu \end{bmatrix} \tag{43}$$

where ν is an angle specifying the unit vectors. Substituting Eqs. (39)–(43) into constraint in Eq. (18) yields

$$\begin{aligned} g(t,\alpha,\beta,\lambda) = \boldsymbol{n}^T[&\Phi_{11}(t-t_s)\boldsymbol{r}_c + \Phi_{12}(t-t_s)\boldsymbol{v}_c \\ &+ \Psi_1(t-t_s)\boldsymbol{u}(\lambda) - \boldsymbol{r}_{\text{ref}} + \Phi_{11}(t)\delta\boldsymbol{r}_0(\alpha) \\ &+ \Phi_{12}(t)\delta\boldsymbol{v}_0(\beta) + \Psi_1(t)\delta\boldsymbol{u}(\lambda)] = 0 \end{aligned} \tag{44}$$

From expressions Eq. (39) and (40), the following partial derivatives are obtained:

$$\frac{\partial[\delta\boldsymbol{r}(t,\alpha,\beta,\lambda)]}{\partial\alpha} = \Phi_{11}(t)\frac{d[\delta\boldsymbol{r}_0(\alpha)]}{d\alpha} \tag{45}$$

$$\frac{\partial[\delta\boldsymbol{r}(t,\alpha,\beta,\lambda)]}{\partial\beta} = \Phi_{12}(t)\frac{d[\delta\boldsymbol{v}_0(\beta)]}{d\beta} \tag{46}$$

$$\begin{aligned} \frac{\partial[\delta\boldsymbol{r}(t,\alpha,\beta,\lambda)]}{\partial t} = \delta\boldsymbol{v}(t,\alpha,\beta,\lambda) &= \Phi_{21}(t)\delta\boldsymbol{r}_0(\alpha) \\ &+\Phi_{22}(t)\delta\boldsymbol{v}_0(\beta) + \Psi_2(t)\delta\boldsymbol{u}(\lambda) \end{aligned} \tag{47}$$

$$\frac{\partial[\delta\boldsymbol{r}(t,\alpha,\beta,\lambda)]}{\partial\lambda} = \Psi_1(t)\frac{d[\delta\boldsymbol{u}(\lambda)]}{d\lambda} \tag{48}$$

$$\begin{aligned} \frac{d\boldsymbol{r}_n(t)}{dt} = \boldsymbol{v}_n(t) &= \Phi_{21}(t-t_s)\boldsymbol{r}_c \\ &+ \Phi_{22}(t-t_s)\boldsymbol{v}_c + \Psi_2(t-t_s)\boldsymbol{u} \end{aligned} \tag{49}$$

Substitute these partial derivatives into Eqs. (21)–(23) to obtain

$$\begin{aligned} \frac{\partial\beta(t,\alpha,\lambda)}{\partial\alpha} = -&\left[\boldsymbol{n}^T\Phi_{12}(t)\frac{d[\delta\boldsymbol{v}_0(\beta)]}{d\beta}\right]^{-1}\boldsymbol{n}^T \\ &\cdot\Phi_{11}(t)\frac{d[\delta\boldsymbol{r}_0(\alpha)]}{d\alpha} \end{aligned} \tag{50}$$

$$\frac{\partial\beta(t,\alpha,\lambda)}{\partial t} = -\left[\boldsymbol{n}^T\Phi_{12}(t)\frac{d[\delta\boldsymbol{v}_0(\beta)]}{d\beta}\right]^{-1}\boldsymbol{n}^T\boldsymbol{V}_r \tag{51}$$

$$\frac{\partial\beta(t,\alpha,\lambda)}{\partial\lambda} = -\left[\boldsymbol{n}^T\boldsymbol{\Phi}_{12}(t)\frac{d[\delta\boldsymbol{v}_0(\beta)]}{d\beta}\right]^{-1}\boldsymbol{n}^T\boldsymbol{\Psi}_1(t)\frac{d[\delta\boldsymbol{u}(\lambda)]}{d\lambda} \tag{52}$$

where

$$\begin{aligned} \boldsymbol{V}_r = &\Phi_{21}(t-t_s)\boldsymbol{r}_c + \Phi_{22}(t-t_s)\boldsymbol{v}_c + \Psi_2(t-ts)\boldsymbol{u} \\ &+ \Phi_{21}(t)\delta\boldsymbol{r}_0(\alpha) + \Phi_{22}(t)\delta\boldsymbol{v}_0(\beta) + \Psi_2(t)\delta\boldsymbol{u}(\lambda) \end{aligned} \tag{53}$$

These results are then substituted into Eqs. (28)–(30) to solve

$$\begin{aligned} \frac{\partial r^p}{\partial t} = &\boldsymbol{p}^T\boldsymbol{V}_r - \boldsymbol{p}^T\Phi_{12}(t)\frac{d[\delta\boldsymbol{v}_0(\beta)]}{d\beta} \\ &\cdot\left[\boldsymbol{n}^T\Phi_{12}(t)\frac{d[\delta\boldsymbol{v}_0(\beta)]}{d\beta}\right]^{-1}\boldsymbol{n}^T\boldsymbol{V}_r \end{aligned} \tag{54}$$

$$\begin{aligned} \frac{\partial r^p}{\partial\alpha} = &\boldsymbol{p}^T\Phi_{11}(t)\frac{d[\delta\boldsymbol{r}_0(\alpha)]}{d\alpha} - \boldsymbol{p}^T\Phi_{12}(t)\frac{d[\delta\boldsymbol{v}_0(\beta)]}{d\beta} \\ &\cdot\left[\boldsymbol{n}^T\Phi_{12}(t)\frac{d[\delta\boldsymbol{v}_0(\beta)]}{d\beta}\right]^{-1}\boldsymbol{n}^T\Phi_{11}(t)\frac{d[\delta\boldsymbol{r}_0(\alpha)]}{d\alpha} \end{aligned} \tag{55}$$

$$\begin{aligned} \frac{\partial r^p}{\partial\lambda} = &\boldsymbol{p}^T\boldsymbol{\Psi}_1(t)\frac{d[\delta\boldsymbol{u}(\lambda)]}{d\lambda} - \boldsymbol{p}^T\boldsymbol{\Phi}_{12}(t)\frac{d[\delta\boldsymbol{v}_0(\beta)]}{d\beta} \\ &\cdot\left[\boldsymbol{n}^T\boldsymbol{\Phi}_{12}(t)\frac{d[\delta\boldsymbol{v}_0(\beta)]}{d\beta}\right]^{-1}\boldsymbol{n}^T\boldsymbol{\Psi}_1(t)\frac{d[\delta\boldsymbol{u}(\lambda)]}{d\lambda} \end{aligned} \tag{56}$$

Thus, the analytical forms of the partial derivatives are obtained. By substituting Eqs. (44), (54)–(56) into Eq. (33), a system of three nonlinear algebraic equations is obtained in the variables α, β, λ, and t, which can be solved numerically at each instant of time by the Newton–Raphson iteration. Then, the boundary of the RRD in the direction of $\boldsymbol{p}$ can be determined by substituting the solved $\boldsymbol{X}^* = [t^*, \alpha^*, \beta^*, \lambda^*]^T$ into Eq. (24).

4. Result

4.1 Simulation Condition

The numerical experiments are conducted for a circular LEO with an altitude of 400 km and inclination of 45 deg. The orbital elements of the chief spacecraft are summarized in Table 1. The deputy shares the same orbit initially, but differs in area-to-mass ratio, leading to a distinct drag response.

Table 1: Orbital parameters of the chief spacecraft.

Semi-major axis a	6778 km
Eccentricity e	0.0
Inclination i	45°
RAAN Ω	90°
Argument of perigee ω	0°
True anomaly f	0°

Table 2: Spacecraft parameters.

	Chief	Deputy
Mass m [kg]	100	150
Area A [m^2]	4.5	0.6
Area-to-mass ratio A/m [m^2/kg]	0.045	0.004
Drag coefficient C_D	2.2	2.2

Atmospheric density is modeled as a constant $\rho = 3.0 \times 10^{-12}$ kg/m^3, corresponding to typical conditions at 400 km altitude [3, 6, 7]. Both spacecraft are assumed to have identical drag coefficients $C_D = 2.2$. The detailed spacecraft parameters are listed in Table 2.

4.2 Reachable Domain Visualization

Figures 6 and 7 illustrate the RRDs for the case of initial position error $\delta r_0 = 10$ m and initial velocity error $\delta v_0 = 0.05$ m/s. Two atmospheric density cases are considered: a nominal value ($\delta\rho = 0\%$) and a perturbed case ($\delta\rho = 30\%$). In the nominal atomospheric density case in Fig. 6, the RRD exhibits a nearly symmetric shape around the nominal trajectory. When density uncertainty is introduced in Fig. 7, the domain is elongated in the along-track direction due to the variation in drag acceleration. This effect highlights that density uncertainty, even at the 30% level, has a dominant influence on the growth of the RRD compared to the initial state uncertainty. As a result, neglecting density uncertainty can lead to underestimation of the relative motion envelope.

In addition to the RRD visualization, Figs. 8–11 show the time histories of the projection distance along the reference-point direction (r_p) and the relative distance between the chief and deputy, respectively. The initial condition is $\delta r_0 = 10$ m, $\delta v_0 = 0.05$ m/s, and two density cases are compared ($\delta\rho = 0\%, 30\%$). In the nominal case ($\delta\rho = 0\%$), both r_p and the relative distance remain bounded within a small range. With density uncertainty ($\delta\rho = 10\%$), however, r_p diverges in the along-track direction, and the overall separation grows monotonically with time. This confirms that the cumulative effect of drag uncertainty is the dominant factor in the long-term relative dynamics.

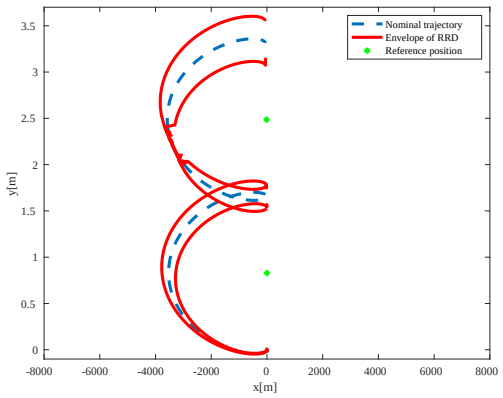

Fig. 6: Comparison of RRD with initial errors $\delta r_0 = 10$ m, $\delta v_0 = 0.05$ m/s, $\delta\rho = 0\%$.

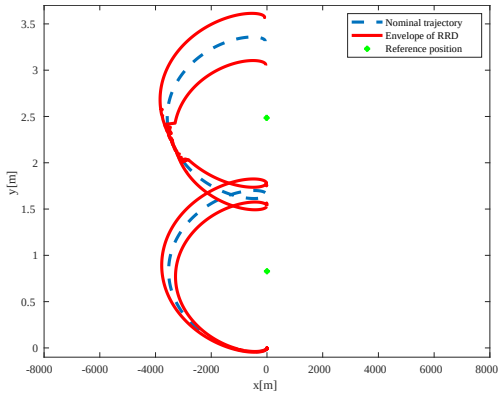

Fig. 7: Comparison of RRD with initial errors $\delta r_0 = 10$ m, $\delta v_0 = 0.05$ m/s, $\delta\rho = 30\%$.

4.3 Monte Carlo Validation

To validate the analytical RRD construction, Monte Carlo simulations were performed with 500 random samples. The initial errors were set to $\delta r_0 = 10$ m and $\delta v_0 = 0.05$ m/s, and the atmospheric density was perturbed as

$$\rho = \rho_0 + \delta\rho, \qquad \delta\rho \sim \tanh(\lambda), \quad \lambda \in [-6, 6],$$

Each sample was propagated using the nonlinear equations of motion with scaled drag accelerations, and the resulting trajectories were compared against the analytical RRD envelope.

Figures 12 and 13 show the Monte Carlo results. The Monte Carlo cloud (light blue dots) and endpoints (black dots) are fully contained within the RRD boundary (red

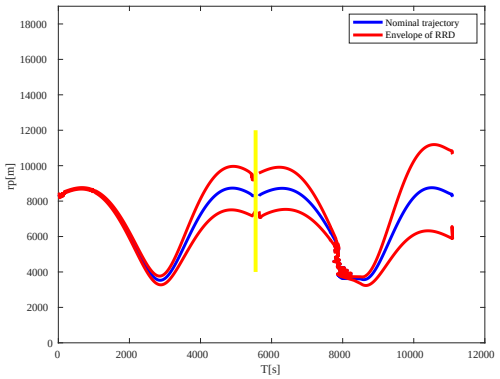

Fig. 8: Time history of the projection distance r_p for $\delta r_0 = 10$ m, $\delta v_0 = 0.05$ m/s, $\delta\rho = 0\%$.

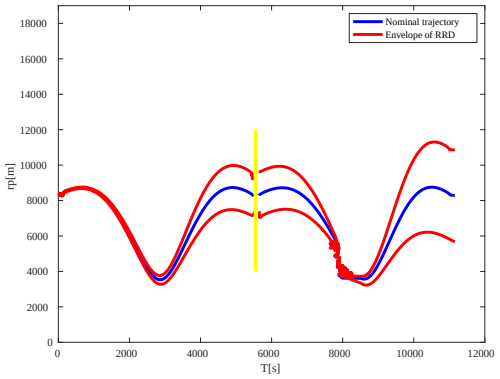

Fig. 9: Time history of the projection distance r_p for $\delta r_0 = 10$ m, $\delta v_0 = 0.05$ m/s, $\delta\rho = 30\%$.

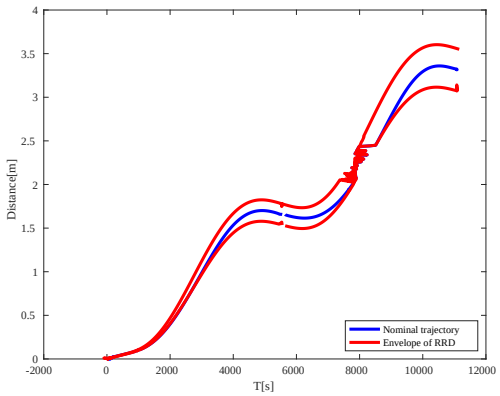

Fig. 10: Time history of the relative distance between chief and deputy for $\delta r_0 = 10$ m, $\delta v_0 = 0.05$ m/s, $\delta\rho = 0\%$.

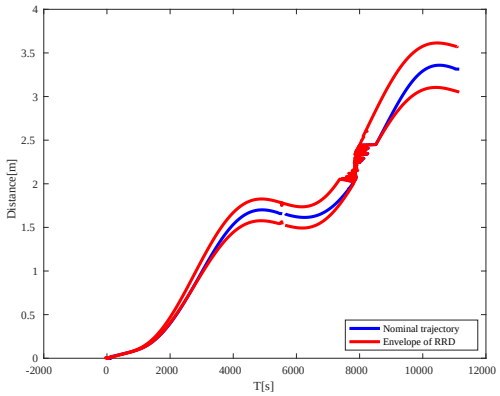

Fig. 11: Time history of the relative distance between chief and deputy for $\delta r_0 = 10$ m, $\delta v_0 = 0.05$ m/s, $\delta\rho = 30\%$.

line), confirming that the proposed RRD provides a conservative outer bound. The sample distribution exhibits elongation in the along-track direction, consistent with the cumulative effect of differential drag under density uncertainty [12].

5. Conclusion

This paper has presented a framework for constructing the relative reachable domain (RRD) of spacecraft in low Earth orbit (LEO) while explicitly considering atmospheric drag. The proposed formulation incorporates differential drag through ECI–LVLH transformations, enabling accurate characterization of relative motion under realistic conditions. Numerical simulations demonstrated that the uncertainty in atmospheric density, even at the 10% level, significantly skews the RRD in the along-track direction. Neglecting this effect leads to underestimation of the reachable set and, consequently, collision risk. Monte Carlo simulations further validated the conservativeness of the RRD, showing that all sample trajectories were contained within the analytical envelope. These results highlight the critical role of drag and density uncertainty in assessing collision risks and formation safety in LEO. The proposed RRD framework provides a practical tool to capture these effects and extend conventional methods beyond drag-free assumptions. Future work will focus on extending the analysis to full three-dimensional relative motion, incorporating empirical density models such as JB2008, and exploring on-board or real-time applications of the RRD for autonomous collision avoidance.

References

[1] J.-C. Liou, "An active debris removal parametric study for leo environment remediation," *Advances in Space Research*, vol. 47, no. 11, pp. 1865–1876, 2011.

[2] S. Isobe, Y. Yoshimura, T. Hanada, Y. Itaya, and T. Fukushima, "Formation keeping control for deorbiting an uncooperative satellite by laser ablation," *Advances in Space Research*, vol. 74, no. 4, pp. 1916–1931, 2024.

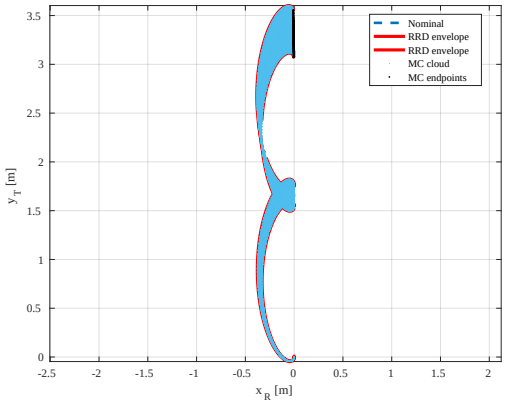

Fig. 12: Monte Carlo validation with 500 samples. Initial errors$\delta r_0 = 10$ m and $\delta v_0 = 0.05$ m/s, $\delta\rho = 0\%$.

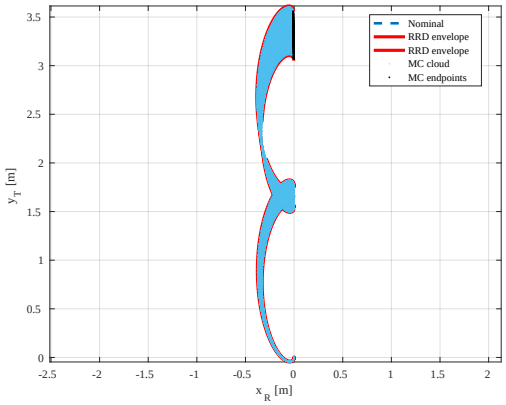

Fig. 13: Monte Carlo validation with 500 samples. Initial errors$\delta r_0 = 10$ m and $\delta v_0 = 0.05$ m/s, $\delta\rho = 30\%$.

[3] G. G. Swinerd, "Air density at heights near 400 km from the orbit of 1963-27a," *Planetary and Space Science*, vol. 30, no. 9, pp. 909–921, 1982.

[4] C. Riano-Rios, R. Bevilacqua, and W. E. Dixon, "Differential drag-based multiple spacecraft maneuvering and on-line parameter estimation using integral concurrent learning," *Acta Astronautica*, vol. 174, pp. 189–203, 2020.

[5] M. K. Ben-Larbi, T. Jusko, and E. Stoll, "Input-output linearized spacecraft formation control via differential drag using relative orbital elements," *Advances in Space Research*, vol. 67, no. 12, pp. 3444–3461, 2021.

[6] J. M. Picone, A. E. Hedin, D. P. Drob, and A. C. Aikin, "Nrlmsise-00 empirical model of the atmosphere: Statistical comparisons and scientific issues," *Journal of Geophysical Research: Space Physics*, vol. 107, no. A12, 2002.

[7] B. R. Bowman, W. K. Tobiska, F. A. Marcos, C.-Y. Huang, C. H. Lin, and W. J. Burke, "A new empirical thermospheric density model jb2008 using new solar and geomagnetic indices," in *AIAA/AAS Astrodynamics Specialist Conference*, 2008.

[8] D. A. Vallado, *Fundamentals of Astrodynamics and Applications*. Microcosm Press, 4th ed., 2013.

[9] D. J. Kessler and B. G. Cour-Palais, "Collision frequency of artificial satellites: The creation of a debris belt," *Journal of Geophysical Research*, vol. 83, no. A6, pp. 2637–2646, 1978.

[10] C. Wen and P. Gurfil, "Relative reachable domain for spacecraft with initial state uncertainties," *Journal of Guidance, Control, and Dynamics*, vol. 39, no. 3, pp. 462–473, 2016. Publisher Copyright: Copyright 2015 by the Authors.

[11] Q. Chen, D. Qiao, and C. Wen, "Reachable domain of spacecraft after a gravity-assist flyby," *Journal of Guidance, Control, and Dynamics*, vol. 42, no. 4, pp. 931–940, 2019.

[12] M. Bando and D. J. Scheeres, "Nonlinear attractive and reachable sets under optimal feedback control in the hill three-body problem," *Journal of Guidance, Control, and Dynamics*, vol. 41, no. 8, pp. 1766–1775, 2018.

[13] S. R. Bowerfind and E. Taheri, "Rapid determination of low-thrust spacecraft reachable sets in two-body and cislunar problems," *arXiv preprint arXiv:2312.08191*, 2023.

[14] B. S. Kumar, A. Ng, K. Yoshihara, and A. D. Ruiter, "Differential drag as a means of spacecraft formation control," *IEEE Transactions on Aerospace and Electronic Systems*, vol. 47, no. 2, pp. 1125–1137, 2011.

[15] M. Shouman, M. Bando, and S. Hokamoto, "Output regulation control for satellite formation flying using differential drag," *Journal of Guidance, Control, and Dynamics*, vol. 42, no. 10, pp. 2220–2236, 2019.